Support Effect and Surface Reconstruction in In_2O_3/*m*-ZrO_2 Catalyzed CO_2 Hydrogenation

Xueqiang Zhang[1+], Alexey V. Kirilin[2], Steve Rozeveld[3], Joo H. Kang[3*], Glenn Pollefeyt[4], David F. Yancey[3], Adam Chojecki[2], Britt Vanchura[3], Monika Blum[1,5*]

[1]*Chemical Sciences Division, Lawrence Berkeley National Laboratory, Berkeley, CA 94720, USA;*
[2]*Core R&D, Dow Benelux B.V., Terneuzen, 4530 AA, The Netherlands;*
[3]*Core R&D, The Dow Chemical Company, Midland, MI 48674, USA;*
[4]*Packaging & Specialty Plastics and Hydrocarbons R&D, Dow Benelux B.V., Terneuzen, 4530 AA, The Netherlands;*
[5]*Advanced Light Source, Lawrence Berkeley National Laboratory, Berkeley, CA 94720, USA*

Corresponding Author

[*]E-mail: mblum@lbl.gov; jhkang@dow.com

Address: 1 Cyclotron Rd., Chemical Sciences Division & Advanced Light Source, Lawrence Berkeley National Laboratory, Berkeley, CA 94720, USA; Core R&D, The Dow Chemical Company, Midland, MI 48674, USA

+Current address: School of Mechanical Engineering, Beijing Institute of Technology, Beijing 10081, China

Abstract

We investigate the chemical and structural dynamics at the interface of In_2O_3/*m*-ZrO_2 and their consequences on CO_2 hydrogenation reaction (CO_2HR) under reaction conditions. While acting to enrich CO_2, *m*-ZrO_2 was also found to serve as a chemical and structural modifier of In_2O_3 that directly governs the outcome of the CO_2HR. These modifying effects include: 1) Under reaction conditions (above 623 K), partially reduced In_2O_3, i.e., InO_x ($0 < x < 1.5$), was found to migrate in and out of the subsurface of *m*-ZrO_2 in a semi-reversible manner, where *m*-ZrO_2 accommodates and stabilizes InO_x by serving as a reservoir. The decreased concentration of surface InO_x under elevated temperatures coincides with significantly decreased selectivity towards methanol and sharp increase of reverse water-gas shift (RWGS) reaction. The reconstruction-induced variation of InO_x concentration appears the one of the most important factors contributing to the altered catalytic performance of CO_2HR at different reaction conditions. 2) The strong interactions and reactions between *m*-ZrO_2 and In_2O_3 result in the activation of a pool of In-O bonds at the In_2O_3/*m*-ZrO_2 interface to form oxygen vacancies. On the other hand, the high dispersity of In_2O_3 nanostructures onto *m*-ZrO_2 prevents their over-reduction under catalytically relevant conditions (up to 673 K), when bare In_2O_3 is unavoidably reduced into metallic phase (In^0). The relationship between the extent of reduction of In_2O_3 and catalytic performance (CO_2 conversion, CH_3OH selectivity, or yield of CH_3OH) suggests the presence of an optimum coverage of surface InO_x and oxygen vacancies under reaction conditions. The conventional model which links catalytic performance solely to the coverage of oxygen vacancies appears invalid in the present case. *In situ* analysis also allows the observation of surface reaction intermediates and their interconversions, including the reduction of CO_3^* into formate, a precursor for the formation of methanol and CO. The combinative *ex situ* and *in situ* study sheds light on the reaction mechanism of the CO_2HR on In_2O_3/*m*-ZrO_2-based catalysts. Our findings on the large-scale surface reconstructions, support effect, and the reaction mechanism of In_2O_3/*m*-ZrO_2 for CO_2HR may apply to other related metal oxide-catalyzed CO_2 reduction reactions.

Key words: In_2O_3/*m*-ZrO_2; support effect; *in situ*; CO_2 hydrogenation; reconstruction; ambient pressure X-ray photoelectron spectroscopy (APXPS)

Introduction

Carbon dioxide hydrogenation reaction (CO_2HR) to form transportable liquid fuels represents a promising way to mitigate the emission of a major greenhouse gas and to generate valuable energy carriers. As a key feedstock for important downstream commodity chemicals and reaction intermediates (formaldehyde, acetic acid, longer-chain hydrocarbons, olefins and gasoline, etc.), methanol is a promising first-step product for the utilization of captured CO_2 ($CO_2 + 3H_2 \rightarrow CH_3OH + H_2O$).[1-3] Currently, methanol is industrially produced by syngas (CO/H_2) using a Cu-ZnO-Al_2O_3 catalyst ($CO + 2H_2 \rightarrow CH_3OH$), which shows significantly decreased catalytic activity in the presence of CO_2 because of the inhibiting effect of water as a byproduct of the competing reverse water-gas shift (RWGS) reaction ($CO_2 + H_2 \rightarrow CO + H_2O$).[4,5] While CO_2HR is kinetically limited at low temperatures, RWGS is often thermodynamically favored at high temperatures.[6,7] Therefore, in order to achieve selective methanol production, CO_2HR must be performed under kinetically-controlled conditions with efficient catalysts, sufficiently low conversion, and optimized adsorption/desorption dynamics of the surface species.

Indium oxide (In_2O_3) has recently been found highly selective for CO_2HR,[5,6,8-22] both theoretically[8-12,17,18,23] and experimentally.[5,6,13-16,18-21,24-27] In particular, Ye et al. investigated the catalytic role of In_2O_3 and the mechanistic reaction pathways for CO_2HR using density functional theory (DFT).[8-12] Pérez-Ramírez group reported catalytic performance of In_2O_3 for methanol synthesis by CO_2HR[5,6] and found that monoclinic zirconia (*m*-ZrO_2), out of many examined supports, sustainably boosts the catalytic performance of In_2O_3 for CO_2HR.[13] The great promise of In_2O_3/*m*-ZrO_2 based catalysts for CO_2HR arises from the respective unique role of In_2O_3, *m*-ZrO_2, and their interactions, which has attracted intense attention recently. For example, in a theory-guided catalytic study, Dang et al. reported the hexagonal In_2O_3 (104) surface as the catalytically active phase.[18] Tsoukalou *et al*. found that unsupported In_2O_3 nanoparticles suffer quick deactivation that coincides with the formation of metallic In (In^0), which leads to non-reversible agglomeration of catalytically active sites.[28] While almost exclusive formation of methanol was found on In_2O_3-based catalysts in early studies,[5] methanol selectivity ranging from 20% to 90% has since been reported.[8,11,14-16,19] By tuning the loading of In_2O_3 onto a ZrO_2 support (0.1 – 5 *wt*%), Chen *et al.* found the stepwise hydrogenation of key reaction intermediate, e.g., *HCOO, and a shift of the products from CO to methanol.[15] In order to probe the unique role of *m*-ZrO_2, Frei *et al.* prepared solid solutions of In_2O_3-ZrO_2 and found no electronic communications

between ZrO_2 and In_2O_3;[13] instead, *m*-ZrO_2 was found to exhibit less favorable epitaxial lattice matching with In_2O_3 and induces tensile strain at the In_2O_3/*m*-ZrO_2 interface that leads to a higher concentration of oxygen-vacancies (O-vacancies) in In_2O_3.[29] It was concluded that the defect chemistry of ZrO_2 could lead to the elucidation of the role of ZrO_2 as a unique support and the reaction mechanism of In_2O_3/*m*-ZrO_2 catalyzed CO_2HR to form methanol.[13]

The promoting effect of *m*-ZrO_2 and the large variation in the reported catalytic performance of In_2O_3/*m*-ZrO_2-based catalysts suggests that CO_2HR is highly sensitive towards the chemical, structural, and electronic details on In_2O_3 surfaces and/or at the In_2O_3/*m*-ZrO_2 interface. Here, we combine various *ex situ* and *in situ* characterizations, including transmission electron microscopy (TEM), catalysis under industrially relevant conditions, ambient pressure X-ray photoelectron spectroscopy (APXPS) and X-ray absorption spectroscopy (XAS) to explore the In_2O_3/*m*-ZrO_2 catalysts in action. It was found that *m*-ZrO_2 plays three distinctive roles under low (below 573 K) and high (above 623 K) reaction temperatures. On the one hand, *m*-ZrO_2 enriches CO_2 on the surface of the catalyst via the formation of surface CO_3^*. It also acts as a "chemical modifier" that simultaneously activates a pool of In-O bonds in In_2O_3 to form oxygen vacancies. Lastly, it acts as a "structural stabilizer" that prevents the over-reduction of In_2O_3 (In^0) via high-dispersity and strong InO_x-*m*-ZrO_2 interactions. At high reaction temperatures (> 623 K), the majority of partially reduced In_2O_3, InO_x ($0 < x < 1.5$), was found to reversibly "dissolve" into the subsurface of *m*-ZrO_2, and the catalyst surface with less In loading promotes the RWGS reaction. The InO_x migrates in and out of the subsurface of *m*-ZrO_2 in a partially reversible manner and thus, governs the outcome of CO_2HR. While bare In_2O_3 is largely reduced into metallic phase at the high reaction temperatures, In_2O_3 supported on *m*-ZrO_2 was partially reduced and only InO_x was observed. In addition, *in situ* analysis allows the direct observation of surface reaction intermediates and their interconversions, shedding light on the reaction mechanism of CO_2HR that is otherwise inaccessible via *ex situ* and non-surface-sensitive approaches.

Methods

Catalysts preparation and catalysis of CO_2HR. The In_2O_3/*m*-ZrO_2 catalysts with various loadings of In_2O_3 were prepared by incipient wetness impregnation of $In(NO_3)_3$ (Sigma Aldrich, stock solution $c_0 = 2$ mol·L^{-1}) onto commercially available 60-80 mesh particles of *m*-ZrO_2 dried under static air (NORPRO SZ31164, S_{BET} 97.9 $m^2 \cdot g^{-1}$ and single-point adsorption total pore volume of

0.27 $cm^3.g^{-1}$). The impregnation solutions were prepared by diluting the stock solution with DI water to provide the same volume with varied amounts of indium precursor. After drying (393 K) and calcination (static calcination oven, ramp 3 $K \cdot min^{-1}$, dwell 4 h at 823 K) the actual loading in In_2O_3 was determined by X-ray fluorescence (XRF) at 0.8, 2.5 and 7.1 wt%. The physical mixture of *m*-ZrO_2 and In_2O_3 (Sigma Aldrich, #632317-5G, BET 3.1 m^2/g) powders were prepared using a quartz mortar to generate a mixture with a nominal In concentration of 7.1 *wt* %. The powder was compacted, crushed and sieved to obtain aggregates of 60-80 mesh and was used in all experiments. The catalysts are denoted as InZr_x (Table 1, x= represents the weight percentage of In).

Table 1 Catalysts used for catalysis of CO_2HR with different nominal loadings of In.

Catalyst (In loading, *wt* %)	Sample code
Monoclinic ZrO_2 (0 *wt* %)	*m*-ZrO_2
In_2O_3/ZrO_2 (0.8 *wt* %)	InZr_0.8
In_2O_3/ZrO_2 (2.5 *wt* %)	InZr_2.5
In_2O_3/ZrO_2 (7.1 *wt* %)	InZr_7.1
In_2O_3 (82.3 *wt* %)	In_2O_3
Physical mixture of ZrO_2 and In_2O_3 (7.1 *wt* %)	InZr_phys

Several catalysts (Table 1) were tested for CO_2HR using a high-pressure parallel fixed bed reactor or PFBR[30] (former Symyx, now UnChained Labs) located in the High Throughput Lab, Chemical Science / Core R&D facility in Terneuzen (Dow Benelux B.V.) and corresponding abbreviations are listed in Table 1. Prior to the catalytic test, quartz microreactors were loaded with either 50 or 100 mg of sieved (60-80 mesh), but one microreactor was only loaded only quartz chips (blank) to monitor the feed composition throughout the experiment. A gas mixture comprised of H_2 (50.9 %), CO_2 (15.7 %), and internal standard He (33.3 %) was fed at 35 bar (3.5 MPa) at a flow of 15 sccm (STP), which corresponds to GHSV of 18000 or 9000 h^{-1} for lower and higher catalyst loading, respectively. The temperature-resolved screening protocol commenced with a prolonged dwell at 523 K (60 h) then moved in 50 K steps up to 673 K and back (controlled ramp rate 10 K min^{-1}) with a 24 h long duration, i.e., the catalysts were tested in a temperature series of

523 K, 573 K, 623 K, 673 K, 623 K, 573 K, 523 K with a heating/cooling rate of 10 K min^{-1} and analyzed by an online Maxum gas chromatograph, equipped with both TCD and FID detectors for permanent gasses and hydrocarbon products respectively. Although the conversion of CO_2 was low at 523-573 K in some catalysts, the catalysis data remains highly repeatable. Relative standard errors below 2% on both conversion and selectivity were observed. Conversion and selectivity were obtained via the following relationship, after averaging catalysis data from two to three trials of experiments under steady-state conditions,

$$Conversion = \frac{F_{CO_2^{in}} - F_{CO_2^{out}}}{F_{CO_2^{in}}} \times 100$$

$$Selectivity = \frac{n \times F_i}{\sum(n \times F_i)} \times 100$$

$$Yield = \frac{n \times Conversion \times Selectivity}{100}$$

Where F_CO2^{in} and F_CO2^{out} represent the molar flow of CO_2 at the inlet and outlet of the reactor, F_i is the molar flow of product i, and n is the number of C atoms in product i. These flows are calculated using the internal standard method. Carbon balance for all experiments were calculated based on the equation below, and was consistently >99%.

$$CB = \frac{\sum n \times F_i + F_{CO_2^{out}}}{F_{CO_2^{in}}} \times 100$$

TEM of In_2O_3/m-ZrO_2 before and after catalysis. Fresh and spent InZr_7.1 (Table 1) catalyst powders were subjected to TEM analysis. The spent catalyst was recovered from an APXPS measurement (after heating at 623 K in the reaction atmosphere) and was vacuum-sealed in a N_2 glovebox to minimize air-exposure and delivered for TEM analysis. The catalyst powder was crushed and dispersed in methanol, prior to drop-casting the solution onto a Cu TEM grid with a lacey carbon support (300 mesh Cu grid, Ted Pella 01883). High-resolution TEM (HRTEM) and High-angle annular dark-field scanning TEM (HAADF-STEM), and energy dispersive x-ray spectroscopy (EDS) were performed on aberration-corrected Thermo-Fisher Titan Themis G2 microscope operated at an accelerating voltage of 200 kV. Conventional TEM images were acquired using a Ceta 4K camera with an exposure time of 1-2 seconds. STEM images were collected at 2048 x 2048 image size, ~100 pA probe current, using a 2 µsec/pixel dwell time (E.A. Fischione Instruments HAADF detector). The Titan 80-300 XFEG TEM/STEM had ChemiSTEM

technology capability with four EDS detectors with an energy resolution of 137eV/channel for EDS mapping. EDS maps were collected at low magnification (10 kx – 40 kx) using 1024x1024 pixel maps with a pixel size of 8nm - 2nm. EDS maps were collected using a dwell time of 12 µsec/ pixel and total collection time of 2000 seconds with probe current of ~ 300 pA. The simulation of HAADF-STEM images was performed using TEMPAS software (Total Resolution, www.totalresolution.com).

APXPS experiment. The APXPS experiments were performed at the undulator beamline 11.0.2.1 of the Advanced Light Source, Lawrence Berkeley National Laboratory. Details of the endstation and the APXPS system have been reported elsewhere.[31,32] Generally, under working conditions, the analysis chamber was filled with reactive gases up to several Torr, which is separated from a differentially pumped electrostatic lens system and a hemispherical electron analyzer (Phoibos 150, Specs) via a physical aperture (0.3 mm, DI). A silicon nitride window (100 nm thick with an active window area of 0.5 mm × 0.5 mm) was used to separate the beamline from the analysis chamber. In a typical experiment, high-resolution photoemission spectra (20 eV pass energy) were recorded with the incident photon energies tuned to ensure a kinetic energy of 200 eV for corresponding outgoing photoelectrons, i.e., 735 eV for O 1s, 640 eV for In 3d, 490 eV for C 1s, and 380 eV for Zr 3d. In_2O_3 powder (Sigma-Aldrich) was used as-received by directly pressing onto an Au foil for APXPS measurement. Because of its poor conductivity of the catalyst powder, differential charging was observed in *m*-ZrO_2-containing samples. To minimize its influence on the quality of the photoemission spectra, Zr photoemission spectra were recorded by drop-casting minimum amount of In_2O_3/*m*-ZrO_2 catalyst powder onto Au foil (50 uL supernatant of 1 mg catalyst powder dispersed in 1 mL ethanol). Sample heating was achieved by electron beam heating of the backside of the heat conductive sample holder, which can heat the temperature of the sample powder up to 1073 K. The sample temperature was measured by a chromel and aluminel thermocouple in direct contact on the top surface. Prior to an APXPS experiment, the catalyst powder was thoroughly degassed by slowly annealing in UHV (< 523 K) and pre-cleaned by annealing in 0.1 Torr of O_2 at 523 K to remove surface carbon species. A typical cleaning process takes ~20 min to totally quench the native C 1s signal; longer treatment time was used for catalyst with lower In_2O_3 loadings, which could be a result of stronger binding of carbon species onto smaller In_2O_3 nanoparticles. The pre-treatment method was carefully optimized for each catalyst to ensure repeatability and minimize inter-sample variations. Note that, although the base pressure of the

analysis chamber was maintained at ~4.0×10^{-10} Torr, adventitious carbon species (284.5 eV) can still be found on the sample surface, which was used for energy calibration. Unless specifically stated, *in situ* catalysis experiment was performed in 0.1 Torr of CO_2 and 0.4 Torr of H_2 between RT and 673 K. SpecsLab2 and CasaXPS software was used for spectral analysis and data processing, where a flexibility of 0.1 eV was typically used for the BE variation and full width at half-maximum (FWHM).

In situ XAS study. X-ray absorption spectroscopy (XAS) measurements were performed at beamline 5BM-D at the Advanced Photon Source (APS) of Argonne National Laboratory. Energy calibration was done using an indium foil (ESPI metal), taking the first inflection point on the In K-edge energy as 27940 eV. Neat catalyst powder was mounted to an *in situ* cell and was subjected to inert and reaction conditions at ambient pressure. During *in situ* measurements, spectra were collected in fluorescence mode at the In K-edge using a passivated implanted planar silicon (PIPS) detector. InZr_7.1 was chosen for the *in situ* XAS measurement. The multiple scans collected at the same condition were averaged and background subtracted using Athena.[33]

UV-vis measurement. The ISR-3100 integrating sphere attachment mounted on the UV-3600 Shimadzu spectrophotometer was used to collect diffuse reflectance spectra of fine powder of samples spread against barium sulfate as a standard. The experiments were performed at a wavelength range of 600 nm to 200 nm, a sampling pitch of 1.0 nm, and under reflectance mode. Based on the changes in the position of the absorption edge it was clear there were differences of the band gap between samples. The acquired diffuse reflectance spectra were converted to Kubelka-Munk function with a quantity $F(R\infty)$ proportional to the absorption coefficient. Thus, the α in the Tauc equation $(h\nu\alpha)^{1/n} = A(h\nu - E_g)$ could be substituted with $F(R\infty)$, where the value of the exponent n denoted the nature of the sample transition. By plotting the Kubelka-Munk function for various n-values against $h\nu$ and finding the point of inflection a line drawn tangent to the point of inflection on the curve of step was constructed. The intersection of the tangent line and the $h\nu$ value at horizontal axis was the band gap E_g value (note: the inflection point was found by taking the first derivative of the curve plotted).

Other characterizations. A Rigaku SmartLab 3kW X-ray diffractometer equipped with a Hypix3000 detector was used to collect diffraction patterns. The samples were examined with copper K_a radiation (λ = 1.541 Å) from a sealed-source tube operated at 40 kV and 44 mA. XRD

data were collected from 5° to 90° 2θ, with a step size of 0.02° and 5 degrees / minute collection time. Analysis of the resulting X-ray diffraction patterns was performed using JADE2010 X-ray pattern analysis software. The thermogravimetric analysis (TGA) was performed on a TGA-Q500 instrument. Samples were dried under N_2 at 423 K for 2 h (ramp rate 10 K/min), prior to cooling down to 313 K. In the presence of flowing gas (10 ml/min N_2 + 90 ml/min air), samples were heated up (10 K/min) from 313 K to 873 K (dwell 2 h) and cooled down to 313 K (10 K/min). Temperature-programmed reduction (TPR) experiments were performed on AutoChem 2920 (Micromeritics) coupled with GSD320 mass spectrometer (MS, Pfeiffer Vacuum). Prior to H_2-TPR, the samples were dried in N_2 at 423 K for 1h. Upon heating up (10 K/min, 10 *vol*% H_2 balanced in Ar), the effluent stream of the instrument was analyzed by MS and thermal conductivity detector (TCD). Because of the very low TCD signal obtained when using a cold trap (*i.e.* low reducibility for supported systems), experiments were performed without a cold-trap and results are shown on the basis of the m/z=18 signal in the MS. A Thermo Scientific DXR2 Raman microscope spectrometer with a 455 nm laser was used to investigate the phonon vibrations of In_2O_3 and In_2O_3/ZrO_2 powders. The samples were prepared for analysis by pouring powders into a shallow aluminum pan and placing on the stage of the microscope. The z-height was manually aligned to achieve the maximal signal-to-noise.

Results and discussions

Characterization of fresh catalysts. Figure 1 shows the characterization of In_2O_3 and In_2O_3/*m*-ZrO_2 catalysts using EDS (Fig. 1a), XRD (Fig. 1b), H_2-TPR (Fig. 1c), TEM (Figs. 1d,1e and Fig. S1) and HAADF-STEM (Fig. 1f). TEM-EDS mapping of the fresh InZr_7.1 catalyst (Fig. 1a and more examples in Fig. S1) at low magnification (large area) indicated a uniform In loading distributed on the *m*-ZrO_2 support with occasional "hot-spots" of In_2O_3 aggregates. The EDS spectra collected from the highlighted areas in Fig. 1a, away from "hot-spot" locations, show an averaged In concentration of 3.9 $\pm$ 0.6 *at* % (Fig. S2). At higher magnification, conventional HR-TEM for InZr_7.1 (Figs. 1d and 1e) recorded away from a "hot spot region" shows no resolvable In_2O_3 nanostructures on the *m*-ZrO_2 support, despite the universal In signal from EDS (Fig. 1d and 1e). The *m*-ZrO_2 nanoparticles were highly crystalline with atomically sharp edges with (111), (2-20), and (1-10) as the mostly observed facets (Fig. 1d and Figs. S3a-b). This suggests that the In_2O_3 nanostructures were highly dispersed on *m*-ZrO_2. We note that Frei et al.[13] reported single-atom

dispersion of In on the *m*-ZrO_2 support using HAADF-STEM (Fig. 1f). We observed similar contrast in InZr_7.1 due to single atoms and clusters using HAADF-STEM (Fig. 1f), but these features may or may not originate solely from In since Hf is also present at a loading of ~ 1wt% in the commercial *m*-ZrO_2 support. A series of STEM images recorded at a "hot-spot" region are shown in Fig. S4, where nanostructures of In_2O_3 up to ~30 nm can be identified. Elemental mapping and small probe EDS of individual ZrO_2 domains indicated In concentrations ranging from 0.4-8.9 *at*% (Fig. S5), but no distinct In_2O_3 nanostructures were detected by TEM or STEM. Therefore, In_2O_3 nanostructures are distributed onto *m*-ZrO_2 via mainly two forms, highly dispersed sub-nanometer clusters indiscernible under TEM or XRD, and nanoparticles with tens of nanometers dimension (at the hot-spots). We note that the detailed structural analysis of the ZrO_2 support was consistent with the characteristics of *m*-ZrO_2, while *t*-ZrO_2 features were not identified using TEM or STEM in the fresh catalyst (InZr_7.1).

Fresh catalyst powders were also characterized by XRD (Fig. 1b), UV-vis diffuse-reflectance spectroscopy (Fig. S6), Raman (Fig. S7), and H_2-TPR (Fig. 1c). XRD patterns of In_2O_3 and In_2O_3/*m*-ZrO_2-based catalysts with respect to standard XRD patterns are shown in Fig. 1b. In addition to diffraction peaks arising from *m*-ZrO_2, features from In_2O_3 can be progressively identified as the loading of In_2O_3 increases. Note that 1) commercially available *m*-ZrO_2 often contains a few percent of *t*-ZrO_2, albeit observed in neither HR-TEM nor Raman spectroscopy; 2) even though the most prominent diffraction peaks of *t*-ZrO_2 and In_2O_3 are both at ~30° (Fig. 1b), the peaks at ~30° in In_2O_3/*m*-ZrO_2 are predominantly from In_2O_3 in "hot spots" as observed by TEM (Fig. S2) and Raman (Fig. S7). The diffractogram of the bare carrier showed no indication of multiphasic ZrO_2 but only its low-temperature monoclinic phase with a characteristic peak (−1 1 1) at ~28.2° (PDF# 00-037-1489). Loading the carrier oxide with progressively higher amounts of indium, the increasing intensity of the feature at 30.6° was associated with the cubic indium oxide (222) phase (PDF# 00-006-0416). Speculatively, if *t*-ZrO_2 phase developed upon In-doping, it might contribute with its strong (011) peak at approximately 30.3° (PDF #00-050-1089). However, both TEM and Raman results pointed to the presence of only the distinctive In_2O_3 phase.

The presence of segregated cubic-In_2O_3 phase, an n-type semiconductor on *m*-ZrO_2 support and a direct band gap insulator, was corroborated with the UV-Vis diffuse-reflectance spectroscopy (Fig. S6), which revealed that the absorptive properties of the series of In_2O_3-ZrO_2 samples gradually increase with In-loading onto the *m*-ZrO_2 surface (Fig. S6b, absorption

expressed with Kubelka-Munk function). *m*-ZrO_2 is characterized with two direct band-to-band transitions, 5.2 and 5.79 eV, [34]. Assuming the direct optical transitions for the In_2O_3-ZrO_2 junction (i.e., n = 1/2 in the Tauc relation) we estimated zirconia-related E_{bg} changed from 5.1 to 4.8 eV for InZr_0.8 and InZr_7.1, respectively (Fig. S6c). Importantly, at the highest concentration of In_2O_3 explored (7.1 wt.%), we could detect an optical transition related to that semiconductor estimated at ~3.4 eV (Fig. S5d). This measurement compares to ~3.63 eV reported by *Qadri et al.* for a thin film In_2O_3 prepared by pulsed-laser deposition and doped with 5 wt% Zr. Furthermore, *King et al.* experimentally measured room temperature (RT) optical gap of the high quality bcc In_2O_3 polymorph (prepared via chemical vapor deposition) at 3.55 ± 0.05 eV.[35] Our measurement of the bulk commercial In_2O_3 powder gave an estimate of ~3.1 eV, which might be explained with the modifying presence of hydroxyl surface species and various grain boundary effects absent in the (virtually) ideal samples of cubic In_2O_3 of the other referenced studies. In some literature reports, indium oxide was described with indirect optical transitions[36] (i.e., by using n = 2 in the Tauc relation, where we would derive E_{bg} of ~2.6 eV based on our measurement over In_2O_3 powder). However, in the view of results generated by extensive density functional theory calculations we should consider In_2O_3 only as a direct semiconductor presenting unusually high conductivity due to the high charge carrier density originated by the oxygen vacancy in the lattice.[37,38] The phonon vibration modes of both *m*-ZrO_2 and In_2O_3 can also be observed by Raman spectroscopy (Fig. S7). Therefore, In_2O_3 primarily exists on *m*-ZrO_2 in two forms, nanoparticles with a size of a few nanometers and highly dispersed In_2O_3; the former is the dominant structure in catalysts with high In loadings, and the latter is the dominate structure in those with lower In loadings. H_2-TPR (Fig. 1c) reveals that the dispersion of In_2O_3 onto *m*-ZrO_2 creates a pool of weaker In-O bonds, in In_2O_3 to form oxygen vacancies at temperature as low as 450-500 K, which would otherwise be inaccessible until ~550 K and above. In fact, the quantity of this kinetically accessible oxygen vacancies is largely enhanced at catalytically relevant temperatures, i.e., 550 K and above, as indicated by the large plateau under the reduction peak. Note that the desorption of native hydroxyls on *m*-ZrO_2 and In_2O_3 can also contribute to the generation of H_2O signal, which leads to the sudden signal rise at ~400 K. Since oxygen vacancies on In_2O_3 are catalytically relevant for CO_2HR, the activation and increase of its pool will ultimately lead to altered catalytic behaviors, as detailed below.

CO_2HR under practical conditions. Figs. 2a and b shows the catalytic performance of 6 catalysts, InZr_0.8, InZr_2.5, InZr_7.1, bare In_2O_3, *m*-ZrO_2, and physical mixture of In_2O_3 and *m*-ZrO_2. Results are displayed in terms of the product distribution (left y-axis), CO_2 conversion (X_{CO2}, right y-axis), and methanol yield (Y_{CH3OH}, Fig. 2c) under different space velocities (18000 or 9000 h^{-1}) and reaction temperatures (a, 523 K; b, 573 K; 623 K and 673 K shown in Fig. S8). Temperatures below 523 K were not investigated because of low X_{CO2}. All the In_2O_3–based catalysts were found highly selective toward methanol at 523 K (80 – 100 %), consistent with other studies.[13,15] Under elevated temperatures, however, the methanol selectivity (S_{CH3OH}) quickly drops to 20 – 60% at 573 K (Fig. 2b) and is almost completely quenched at 623 K and 673 K (Fig. S7), where the formation of CO (S_{CO}) dominates via RWGS. Neither CO nor methanol was observed on pure *m*-ZrO_2 at 523 K; the selectivity towards methanol gradually increases at 573 K and above but remains well-below those of In_2O_3–based catalysts. Notably, a physical mixture of In_2O_3 and *m*-ZrO_2 (P-In_2O_3-*m*-ZrO_2, 7.1 *wt. %* In loading) exhibits a two-stage catalytic performance, it initially resembles bulk In_2O_3 but is similar to InZr_7.1 at high temperatures (Fig. 2 and Fig. S8), suggesting the formation of an In_2O_3-*m*-ZrO_2 interface that uniquely defines In_2O_3/*m*-ZrO_2. In addition, selectivity towards CH_3OH was found highly dependent on the space velocity and X_{CO2}; higher space velocity (18000 h^{-1}), i.e., lower residence time, and X_{CO2} unequivocally lead to higher selectivity towards CH_3OH (Figs. 2a and b).

The catalytic performance of In_2O_3/*m*-ZrO_2 was found to be dependent on In-loading with higher In content, i.e., with large average size of In_2O_3 nanostructures, leading to higher X_{CO2} and higher S_{CH3OH}. This is consistent with the earlier study by Chen et al,[15] where the effect of In-loading was systematically investigated, corresponding to In-loading from InZr_0.24 to InZr_24.4 in the present study. Note that the selectivity towards CH_3OH was found to depend on In-loading and gradually saturates between InZr_6.1 and InZr_24.4. Here, the highest In-loading investigated was InZr_7.1, in the vicinity of optimized range. Notably, at the lower end of In-loading, more In-loading (large average In_2O_3 particle size, i.e., *m*-ZrO_2-aggregated InO_x) leads to better catalytic performance in terms of X_{CO2} and selectivity towards CH_3OH, approaching that of bulk In_2O_3, while the latter has less CO_2 conversion because of a balance between In-loading and exposed active sites. We would like to emphasize that correlation between In-loading and the altered catalytic performance is intrinsically a result of the formation and distribution of catalytically active InO_x species, which is directly related to the size and distribution of initial In_2O_3

nanostructures on *m*-ZrO_2. Thermodynamic analysis of (reverse) water-gas shift reaction (Table S1 and Fig. S9) suggests that neither bulk In_2O_3 nor the supported catalyst (InZr_7.1) reached eq. conversion conditions. Bulk In_2O_3 was found more selective for methanol synthesis but less active, while the supported catalyst (InZr_7.1) shows higher activity and lower selectivity due to RWGS reaction. In particular, Q (RWGS) of InZr_7.1 were found below K_{eq} (RWGS) across the T range, indicating a high water-gas shift activity; On the other hand, Q of In_2O_3 was higher than the K_{eq} at 573 K and 623 K, pointing to its relatively low activity for the RWGS reaction.

While the exact values of X_{CO2} and S_{CH3OH} vary across different studies of In_2O_3-based catalysts,[5,8,11,13,15] catalytic performance evaluated by Y_{CH3OH} (3-4%) in the present study is comparable with state-of-the-art In_2O_3-based catalysts.[5,13] Y_{CH3OH} is a result of the compromise between X_{CO2} and S_{CH3OH} that give rise to a "volcano" shaped relationship as a function of the reaction temperature (Fig. 2c). On one side, this indicates a qualitatively identical reaction mechanism for these catalysts and on another suggests the inaccuracy in the evaluation of catalytic performance solely based on S_{CH3OH}, which is often adversely dependent on X_{CO2} in CO_2HR. In fact, Y_{CH3OH} appears a more practical and robust parameter as it is directly linked with the efficiency of CO_2 transformation into methanol. As shown in Fig. 2c, Y_{CH3OH} of In_2O_3/*m*-ZrO_2 at the optimum condition (573 K) is more than twice that of bare In_2O_3 (623 K), suggesting the importance of *m*-ZrO_2 in promoting the overall catalytic efficiency of In_2O_3 by lifting X_{CO2}.

In situ spectroscopy. To probe the reaction mechanism of CO_2HR catalyzed by In_2O_3/*m*-ZrO_2 catalysts, the interfacial chemical, structural and electronic properties of bare In_2O_3 (Figs. 3a), InZr_2.5, and InZr_7.1 (Figs. 3b-d) were investigated under reaction conditions using APXPS and XAS. Figs. 3a and 3b shows the evolution of In $3d_{5/2}$ photoemission spectra of In_2O_3 powder and InZr_7.1 under various reaction conditions. A symmetric In $3d_{5/2}$ peak at 445.2 eV and the peak at ~530.3 eV in the O 1s spectrum (Fig. S10a) is consistent with the chemical identity of In_2O_3.[39,40] Upon the introduction of 0.1 Torr CO_2, except the appearance of a small O 1s shoulder at ~532.5 eV and a C 1s contribution at 288-289 eV indicating the formation of CO_3^* (Fig. S10b),[41-43] no identifiable change can be observed in In $3d_{5/2}$ (Fig. 3a). This suggests a low coverage of CO_3^* onto In_2O_3 and/or its overlapped photoemission contribution with that of In_2O_3. Substantial spectral changes were observed upon the introduction of H_2 (0.4 Torr). For the photoemission spectra of In $3d_{5/2}$, a broadening and shifting by ~0.3 eV towards the lower BE side was observed,

corresponding to the reduction of In_2O_3 and the formation of InO_x ($0 < x < 1.5$). When temperature reaches 573 K and above, a new peak fingerprinting the formation of In^0 emerged at 444.3 eV.[44,45] More than half of the surface region In atoms were found reduced into metallic state at 623 K, as also confirmed by the progressively quenched O 1s photoemission spectra (Fig. S10a).

Fig. 3d displays representative fitted photoemission spectra of In $3d_{5/2}$ recorded on bare In_2O_3 and InZr_7.1 at 573 K in the reaction atmosphere. While only In_2O_3 and InO_x were observed in InZr_7.1, ~20 % of In in the surface region of bare In_2O_3 is in the form of In^0. This proportion increases at elevated temperatures (up to 70 % at 673 K). The APXPS study on bulk In_2O_3 and the formation of In^0 yields consistent result with *in situ* XAS reported by Tsoukalou *et al.*[28] The redox behavior of In_2O_3 was fully reversible (Fig. 3a) and is therefore only accessible by an *in situ* technique. As reported by Tsoukalou *et al.,*[28] the formation of metallic In was in direct correlation with the deactivation process of In_2O_3 catalyst for CO_2 hydrogenation reaction; the regeneration of largely reduced In_2O_3 catalyst leads to an increase of the average crystallite size of the catalyst. The almost reversely monotonic correlation between In^0 *at* % and S_{CH3OH} (Fig. S11) suggests the negative effect of In^0 on the catalytic performance of InZr_7.1 (Fig. S11a), although Y_{CH3OH} (much lower values than In_2O_3/*m*-ZrO_2 catalysts) also exhibits a volcano relationship with the production of In^0 (Fig. S11b).

Different chemistry was observed *in situ* at the In_2O_3/*m*-ZrO_2 interface. As shown in Fig. 3b, the spectral intensities and peak positions of In $3d_{5/2}$ dynamically evolve in a partially reversible manner. The peak center at ~445.2 eV of In $3d_{5/2}$ suggests a chemical identity of In_2O_3 in InZr_7.1. The introduction of the reaction atmosphere and an increase of temperature (≥ 573 K) leads to a progressive spectral shift from 445.2 eV to 444.9 eV, indicating the partial reduction of In_2O_3 and the formation of InO_x ($0 < x < 1.5$), the catalytically active phase that is responsible for the turn-over of CO_2HR (Fig. 2). As a control test, pre-reduced In_2O_3/*m*-ZrO_2 was found to exhibit enhanced catalytic performance at 523 K than the same catalyst without pretreatment (Fig. S12). In addition, the surface redox behavior and spectral intensity change was largely reversible over the course of three cycles of heating and cooling between 523 K and 673 K. Higher temperature unequivocally leads to enhanced partial reduction of In_2O_3, which can be recovered while the reaction temperature decreases. Remarkably, no metallic phase In was observed throughout the APXPS experiments, suggesting that the In_2O_3 nanoparticles were chemically stabilized by loading onto *m*-ZrO_2. As shown below, the In_2O_3 and *m*-ZrO_2 interactions is beyond typical

physical interactions; in fact, lattice inter-mixing was observed under reaction conditions, which further enhances the chemical and electronic communications at the interface. On the other hand, *m*-ZrO_2 was also found to be chemically stabilized by the loading of In_2O_3 (Fig. S13), as compared with bare ZrO_2, which can be auto-reduced in an inert or reducing environment (Fig. S14).

Remarkably, a partially reversible spectral intensity change can be clearly observed (Fig. 3b), indicating a variation of In concentration at the near surface region. Calculated atomic ratio of Zr/In (Fig. 3c) confirms the dynamic evolution of surface In concentrations, as a result of large scale reconstruction of surface InO_x under a reaction atmosphere. The In $3d_{3/2}$ spectral intensity and therefore the Zr/In ratio can be completely recovered by annealing in 0.1 Torr of O_2 at 573 K, suggesting that the depletion of In content under reaction conditions was a result of inward migration of InO_x into the subsurface of *m*-ZrO_2, or the formation of InO_x domains with significantly increased size and therefore altered distribution of catalytically active sites, instead of leaching/evaporation under high temperatures. The latter scenario was determined unlikely as determined by the extent of signal decrease in In $3d_{5/2}$ (Figs. 3b and 3c) and the TEM analysis of the catalyst before and after reaction.

The spectral changes in In $3d_{3/2}$ demonstrate the continuous shuttling of InO_x in and out of the ZrO_2 subsurface as a function of the reaction temperature and the extent of reduction of In_2O_3. At high temperatures (673 K), the Zr/In atomic ratio of InZr_2.5 and InZr_7.1 were almost identical, corresponding to ~1.5 *at* % of InO_x, likely suggesting an equilibrium of surface reconstruction and the achievement of an optimum concentration of InO_x on the surface. The surface reconstruction was kinetically limited at low temperatures (<573 K) and activated at elevated temperatures upon the large-scale formation of InO_x that has higher surface free energy than bulk In_2O_3.[46] Note that the reaction temperature was well below the melting point of In_2O_3 (2183 K);[47] In_2O_3 residing in the subsurface of ZrO_2 either segregates or forms In_2O_3-ZrO_2 solid solution, as will be discussed below in the microscopic study. Due to configurational limitation of the differential pumping stage, a mass spectrometer was only be installed at the 2nd stage, two chambers away from the analysis chamber, where the sample was heated and in-situ analyzed. The detection of CO or CH_3OH products was attempted but was not successful because of the low concentration. Analysis of O 1s spectra from In_2O_3/ZrO_2 (Fig. S15) is out of the scope of the present study, due to the complexity of its origin, especially since spectral changes originating from In_2O_3 are always overwhelmed by those from ZrO_2. Notably, in a separate study, as will be

reported elsewhere, similar InO_x reconstruction process at the interface was observed for In_2O_3 thin film deposited onto ZrO_2/Zr foil by APXPS under reaction atmosphere, consistent with the phenomena observed in the present In_2O_3/*m*-ZrO_2 system.

To further explore the *in situ* chemistry of In_2O_3/*m*-ZrO_2 catalysts for CO_2HR, XAS was used to gain insight on the oxidation state and coordination environment of In under various reaction conditions (Figs. S16a and b). Consistent with the APXPS analysis, the In_2O_3 nanoparticles on *m*-ZrO_2 experience progressive reduction and form InO_x over the course of temperature increment from RT to 663 K, where In^0 was not observed. As an increase of temperature in the reaction atmosphere, the XANES spectra of In K-edge show an intensity decrease in the white line and a slight shift of the X-ray absorption edge towards lower energy, indicating the reduction of In_2O_3. In addition, the Fourier transformed EXAFS shows two peaks at 1.8 Å and 3.3 Å correspond to the In-O and In-In shell, respectively (Fig. S16b).[28] The decrease in the amplitude of these two shells under reaction conditions are consistent with those observed by Tsoukalou et al., in correlation with the reduction of In_2O_3 (creation of surface oxygen vacancies) and a decrease of atomistic orderliness.[28] In addition to the reaction atmosphere, InZr_7.1 sample was also exposed to N_2 under elevated temperatures, but no significant auto-reduction behavior was found, except certain degree of atomistic disorder (Figs. S16c and d).

Typically, the promoting effect of co-catalysts or supports are ascribed to their capability to enhance the coverage of oxygen vacancy on In_2O_3, which is widely considered as the catalytically active phase under reaction conditions. We have quantified oxygen vacancy generated in the near-surface region of In_2O_3 based on the quantitatively analysis of the In 3d photoemission spectra (Fig. 4a). One can clearly see the two stages of the kinetics of O-vacancy coverage, for InZr_7.1, a quick jump from 523 to 573 K and relatively stabilized coverage from 573 K to 673 K is observed; for In_2O_3, the coverage of O-vacancy is much smaller and exhibits a first increase and then decrease kinetics before and after 573 K. Overall the O-vacancy coverage in In_2O_3 is heavily linked to the formation of metallic phase In and the collapse of original In_2O_3 crystal structure. If the model of oxygen vacancy-driven CO_2HR stands, monotonic correlations between the coverage of oxygen vacancy and S_{CH3OH} or Y_{CH3OH} would be anticipated. However, as shown in Figs. 4b and 4c, no clear correlation can be identified between the quantities of In_2O_3 (*at* %, adversely related to the coverage of oxygen vacancy) and S_{CH3OH} (Fig. 4b) or Y_{CH3OH} (Fig. 4c and Fig. S11). In fact, under certain conditions (Fig. 4b), less oxygen vacancy seems corresponding to higher

Y_{CH3OH}. Although there was a significant pressure gap between APXPS (mbar range) and catalysis (3.5 MPa) experiments, we believe that there are other factors, together with the coverage of oxygen vacancy, affecting the catalytic performance of the In_2O_3-based catalyst in the present catalytic system.

In fact, we believe another important factor is the surface reconstruction under elevated temperatures in the reaction atmosphere (at and above 623 K, Figs. 3b and 3c) for the following reasons: 1) The sudden S_{CH3OH} and Y_{CH3OH} drop between 573 K and 623 K (arrows in Figs. 4b and 4c) coincides with the occurrence of the large-scale surface reconstruction; 2) Based on the catalysis data (Fig. 2), there is an apparent switch of the reaction pathway from CO_2HR to RWGS above 573 K, which is very likely a result of the surface reconstruction that leads to a decrease of InO_x *at*%. As reported in other studies,[15] lower surface concentration of InO_x promotes RWGS and lowers S_{CH3OH}. Collectively, in In_2O_3/*m*-ZrO_2 catalysts, the catalytic performance is governed both by the coverage of oxygen vacancy and the concentration of InO_x under reaction conditions.

TEM analysis of spent In_2O_3/m-ZrO_2 catalysts and strong In_2O_3-m-ZrO_2 interactions. Characterization of the fresh catalyst indicated that In_2O_3 was dispersed on *m*-ZrO_2 as both nanoclusters (Figs. 1 and S3) and larger nanoparticles and aggregates (i.e., hot spot areas, Fig. S2). The spent InZr_7.1 catalyst showed similar features in terms of the large-scale In distributions and nanoparticle aggregates (Figs. S17, S18, and S19), while new In_2O_3 nanostructures were observed in the spent In_2O_3/*m*-ZrO_2 catalyst.

HAADF-STEM images of a In_2O_3 nanoparticle on the spent InZr_7.1 catalyst is shown in Figs. 5a - 5c. Higher resolution HAADF-STEM images of the nanoparticle showed lattice plane spacings consistent with In_2O_3 and the EDS map showed higher In concentration coincident with the nanoparticle. The alternating bright contrast on (400) planes in the experimental image was reproduced in the simulated STEM image (Fig. 5c inset). A line profile across the lattice fringe (Fig. 5c, arrow) shows an alternating contrast that is consistent with the simulated STEM image of In_2O_3 (Fig. 5d). For comparison, the simulated STEM image of *t*-ZrO_2 (inset Fig. 5e) will have similar inter-plane spacings (*t*-ZrO_2 d_{110} = 2.53 Å) and therefore we note that this is a possible match to the experimental image; however, we conclude that *t*-ZrO_2 is a less probable match due to the elevated In levels associated with the nanoparticle and since the STEM image of *t*-ZrO_2 must have equal contrast across all directions (Fig. 5e).

HAADF-STEM images and corresponding element maps such as shown in Fig. S17 shows unique nanostructures similar to those reported by Frei et al., who attributed these features to In incorporated into the *m*-ZrO_2 lattice.[13] This suggests that the bright features originated from In_2O_3 clusters, although the contrast appears more consistent with a higher atomic number such as Hf, which distribute in a homogeneous manner throughout the *m*-ZrO_2 support (Fig. S20). Small In_2O_3 nanoclusters are generally sensitive towards electron beam irradiation;[28,48] however, the In_2O_3 nanoparticle (Figs. 5a-5c) was stable under electron beam irradiation, suggesting a stabilization effect via direct contact with *m*-ZrO_2. We believe that the newly formed In_2O_3 structures were formed during the surface reconstruction process under reaction conditions. It has been reported that incorporation of In into ZrO_2 will stabilize the *t*-ZrO_2 structure,[13] but an increase in the amount of *t*-ZrO_2 was not detected by XRD (Fig. S21). In addition, no In^0 was observed in the spent In_2O_3/*m*-ZrO_2 catalysts under the industrial reaction condition, further suggesting a stabilization effect of *m*-ZrO_2 to avoid over-reduction of InO_x under elevated pressures and temperatures.

Role of m-ZrO_2 and reaction mechanism. The catalysis, *in situ* spectroscopy and TEM studies suggest that *m*-ZrO_2 has multiple roles in the CO_2HR reaction. Besides enhancing the uptake of CO_2, *m*-ZrO_2 also serves as a chemical and structural modifier of In_2O_3 that directly governs the outcome of CO_2HR. The uniqueness of *m*-ZrO_2 as a support for CO_2HR, outperforming many other commonly used supports arises from its strong interactions or even reactions at the In_2O_3 (or InO_x)/*m*-ZrO_2 interface. On one hand, the dispersion of In_2O_3 onto *m*-ZrO_2 and the formation of In_2O_3 (or InO_x)/*m*-ZrO_2 interface weakens a pool of In-O bonds to form oxygen vacancies and simultaneously prevents the over-reduction of In_2O_3 (In^0) in catalytically relevant conditions (up to 673 K). On the other hand, when the reaction temperature is above 623 K, partially reduced In_2O_3, InO_x ($0 < x < 1.5$), was found to "dissolve" into the subsurface of *m*-ZrO_2 in a partially reversible manner and the reaction pathways switches from favoring CH_3OH production to CO formation via RWGS. This trend is consistent with those reported by Chen et al.[15] in terms of the relationship between In concentration and selectivity of CO_2HR. The surface reconstruction and the modified In/Zr atomic ratios can be completely restored by annealing the catalyst in O_2 atmosphere (Fig. 3c). Consistent with the *in situ* spectroscopic study, steady-state catalysis also suggests that the loadings of In in In_2O_3/*m*-ZrO_2 directly govern the reaction pathway of CO_2HR, i.e., the formation of methanol or CO and H_2O via RWGS. We found that *m*-ZrO_2

serves as a reservoir for InO_x under reaction conditions, allowing the shuttling of InO_x in and out of its subsurface in a reducing atmosphere. The CO_2HR process is accompanied by the dynamic structural reconstructions at the In_2O_3 (or InO_x)/*m*-ZrO_2 interface, where the InO_x nanostructures were constantly formed and "dissolved" under specific reaction conditions, by compromising the high chemical potential of InO_x on *m*-ZrO_2 surface (versus subsurface and bulk of *m*-ZrO_2) and the high surface free energy of InO_x (versus In_2O_3). To design more efficient and recyclable catalyst for CO_2HR, the challenge ahead would be to effectively modulate the surface concentration of InO_x under reaction conditions.

APXPS allows the observation of surface reactive species including CO_3^*, formate/carboxyl, methoxyl, and their evolution and interconversions, shedding light on the interpretation of the reaction mechanism at a molecular level. Fig. 6a displays the evolution of C 1s core-level photoemission spectra recorded on InZr_7.1 under various conditions. A qualitative summary of the reaction mechanism pathway on bulk In_2O_3 and In_2O_3/*m*-ZrO_2 with low and high loadings of In is shown in Fig. 7. The adsorption of CO_2 leads to the formation of CO_3^* with a BE of ~290 eV. Although the dissociative adsorption of H_2 onto In_2O_3/*m*-ZrO_2 cannot be directly probed, the partial reduction of In_2O_3 (Fig. 3) and the preservation of CO_3^* on *m*-ZrO_2 in reaction atmosphere suggests its adsorption and dissociation on In_2O_3. Thermogravimetric analysis (TGA) of spent InZr_0.8, InZr_2.5, InZr_7.1, and bulk In_2O_3 (Figs. S22 and S23) demonstrates that more carbonaceous species were adsorbed on *m*-ZrO_2 involving catalysts than bulk In_2O_3, with a total weight loss of 0.6 wt%, 0.7 wt% and 1 wt% of carbon for InZr_0.8, InZr_2.5 and InZr_7.1 respectively, compared to 0.4wt% for bulk In_2O_3 and 1.2 wt% for bare ZrO_2. We believe catalysts with the incorporation of *m*-ZrO_2 have more adsorption of CO_2 onto their surface, where *m*-ZrO_2 serves as a CO_2 adsorber under CO2HR conditions, consistent with our understanding of the reaction mechanism, where CO_2 adsorbs onto *m*-ZrO_2 first, prior to reduction by H* split by In_2O_3. As shown in Fig. S10, without the presence of In_2O_3, CO_2 adsorbs onto ZrO_2 to form carbonate and stops from being converted further. The spillover of H^* to the In_2O_3/*m*-ZrO_2 interface or *m*-ZrO_2 leads to the reduction of CO_3^* and the formation of formate ($HCOO^-$) or carboxylic (-COOH), key intermediates for the formation of methanol and CO, respectively (Fig. 6b). Remarkably, the formation of CO_3^* and its transformation to $HCOO^-$ or –COOH was captured in the C 1s photoemission spectra with their relative atomic ratios highlighted (Fig. 6a). The reaction intermediates were eventually converted into either CO via the dissociation of –COOH or

methanol via further hydrogenation of $HCOO^-$ to form $–OCH_3$ (Fig. 6b). A representative C 1s photoemission spectrum was fit for the quantification of CO_3^*, and $HCOO^-$ and/or –COOH (Fig. 6b).

Conclusions

We report a spectroscopic *in situ* study of the evolution and dynamics of the chemical, structural, and electronic properties at the In_2O_3/*m*-ZrO_2 interface and its consequences on CO_2HR. Systematic investigation by combining catalysis, *in situ* spectroscopy and microscopy leads to the understanding of the mechanism describing In_2O_3/*m*-ZrO_2 catalyzed CO_2HR, the revelation of the role of *m*-ZrO_2 as a unique support, and the first time observation of large-scale reconstructions under reaction conditions. In addition to enriching CO_2 at the catalytic center via conversion into CO_3^*, *m*-ZrO_2 was found to prevent the over-reduction of In_2O_3 to metallic In, serves as a reservoir for InO_x under reaction conditions that allows the shuttling of InO_x in and out of its subsurface via means of continuously inducing InO_x surface segregation and re-dispersion into the lattice of *m*-ZrO_2. In the former scenario, the InO_x nanostructure was found to be stabilized by forming strong In_2O_3-*m*-ZrO_2 interactions and even reactions. At high temperatures, the majority of InO_x was found to reside in the subsurface of ZrO_2 by forming In_2O_3/*m*-ZrO_2 nanocomplex because of its high surface free energy, and the resulting low surface indium concentration leads to increased selectivity towards CO via RWGS. The reconstruction induced variation of InO_x concentration appears the fundamental reason of the altered catalytic performance of CO_2HR at different reaction temperatures. *In situ* analysis also allows the direct observation of surface reaction intermediates and their interconversions, shedding light on the reaction mechanism of CO_2HR that is otherwise inaccessible via *ex situ* and non-surface-sensitive approaches. The present study predicts that an effective modulation of InO_x concentration on *m*-ZrO_2 under reaction conditions could ultimately govern the practical applicability of In_2O_3-based catalysts for CO_2HR. Our findings of *in situ* surface reconstructions and the mechanistic insights of In_2O_3/*m*-ZrO_2 for CO_2HR may apply to general metal oxide catalyzed CO_2 reduction reactions.

Associated Content

Figures S1 – S23 and Table S1 provide additional information as described in the main manuscript.

Acknowledgment

The Advanced Light Source is supported by the Director, Office of Science, Office of BES, of the US DOE under Contract DE-AC02-05CH11231. M.B. was partially supported by the Condensed Phase and Interfacial Molecular Science Program in the Chemical Sciences Geosciences and Biosciences Division of the Office of Basic Energy Sciences of the U.S. Department of Energy under Contract No. DE-AC02-05CH11231. Portions of this work were performed at the DuPont-Northwestern-Dow Collaborative Access Team (DND-CAT) located at Sector 5 of the Advanced Photon Source (APS). DND-CAT is supported by Northwestern University, The Dow Chemical Company, and DuPont de Nemours, Inc. This research used resources of the Advanced Photon Source, a U.S. Department of Energy (DOE) Office of Science User Facility operated for the DOE Office of Science by Argonne National Laboratory under Contract No. DE-AC02-06CH11357.

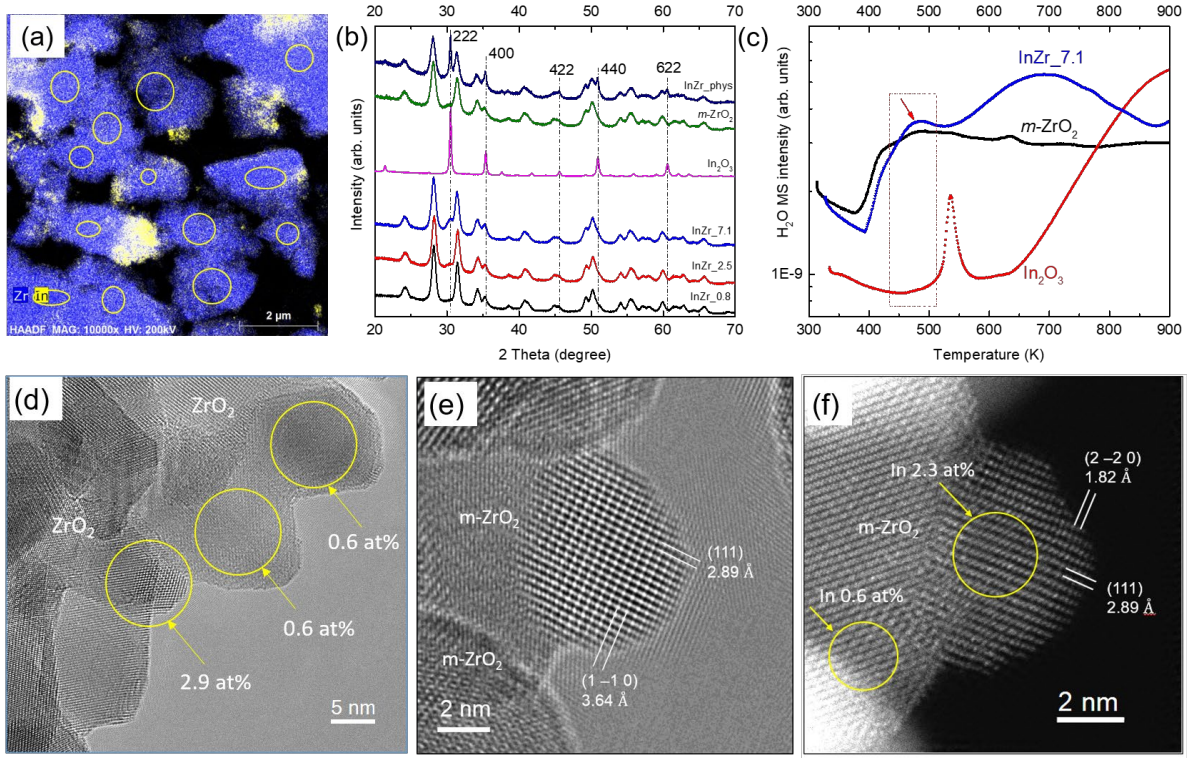

Fig. 1 Characterization of fresh In_2O_3/ZrO_2. a) Representative EDS mapping of the fresh InZr_7.1, where the circled areas were subject to EDS analysis and an averaged In concentration of 3.9±0.6 *at* % was obtained (Fig. S2). b) XRD patterns of In_2O_3, In_2O_3/ZrO_2 with different loadings of In, and physical mixture of In_2O_3 and ZrO_2 powder. Diffraction peaks arising from In_2O_3 are denoted by vertical lines. c) H_2-TPR thermograms of *m*-ZrO_2, In_2O_3, and InZr_7.1. d) and e), HR-TEM images of a fresh InZr_7.1 sample taken at the highlighted "non-hot spot regions" with the inhomogeneous distributions of In. f) HAADF STEM image and EDS of the region shown in e). No In nanoparticles were found in the non-hot spot areas and all the visible nanostructures were of *m*-ZrO_2 nature.

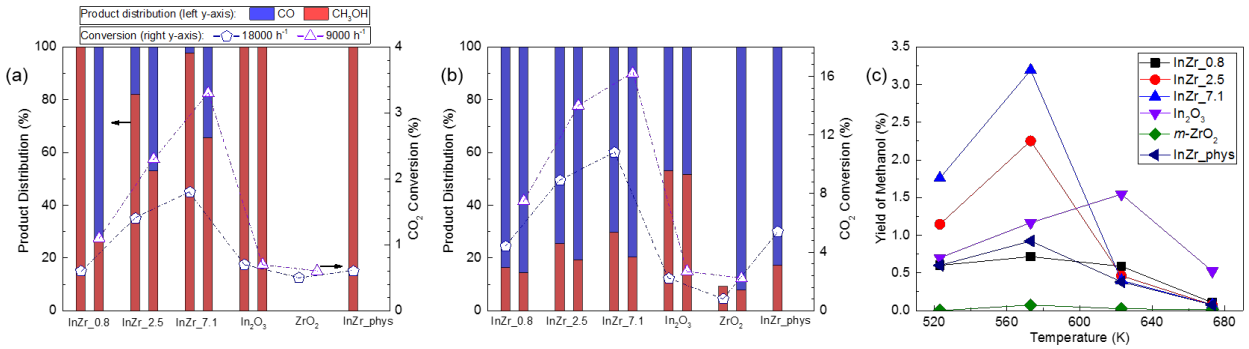

Fig. 2 Catalytic performance of In_2O_3-based catalysts with different In loadings onto a ZrO_2 support or a physical mixture of ZrO_2 and In_2O_3 for CO_2HR. Panels a and b represent catalytic performance of all catalysts at 523 K and 573 K, respectively (those for 623 K and 673 K are shown in Fig. S8). Except the physical mixture (18000 $cm^3/g\_cat^{-1}\ h^{-1}$), all catalysts were measured both under GHSVs of 18000 and 9000 $cm^3/g\_cat^{-1}\ h^{-1}$. Distribution of products was used as the left y-axis and CO_2 conversion (X_{CO2}) is used as the right y-axis. Panel c displays the yields of methanol for different catalysts as a function reaction temperature (GHSV =18000 $cm^3/g\_cat^{-1}\ h^{-1}$).

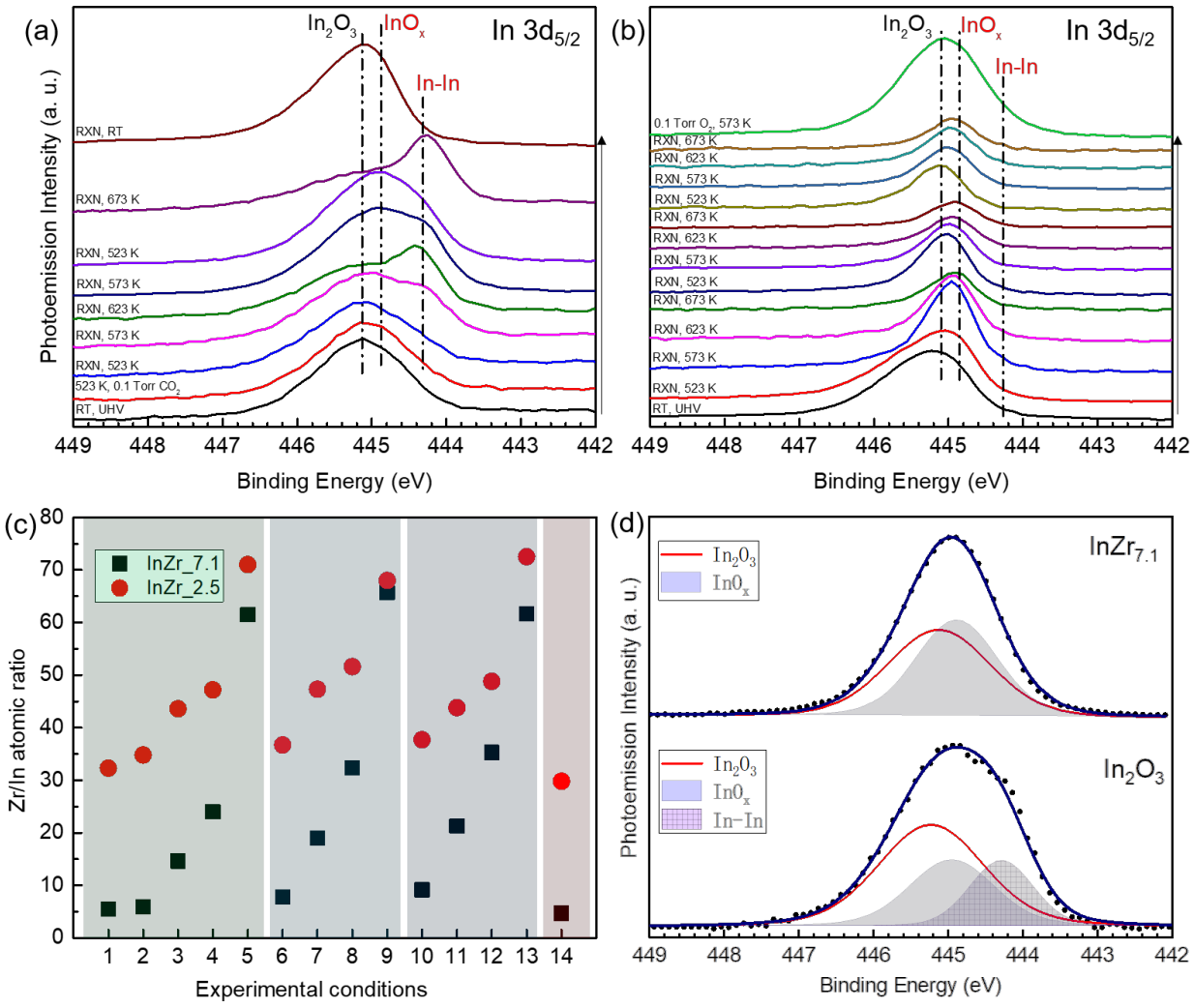
(a)
In 3d5/2
In2O3
InOx
In-In
RXN, RT
RXN, 673 K
RXN, 523 K
RXN, 573 K
RXN, 623 K
RXN, 573 K
RXN, 523 K
523 K, 0.1 Torr CO2
RT, UHV
Photoemission Intensity (a. u.)
Binding Energy (eV)
(b)
In 3d5/2
0.1 Torr O2, 573 K
(c)
InZr_7.1
InZr_2.5
Zr/In atomic ratio
Experimental conditions
(d)
In2O3
InOx
In-In
InZr7.1
Photoemission Intensity (a. u.)
Binding Energy (eV)

Fig. 3 Surface chemical and structural properties probed by APXPS under *in situ* conditions. a) and b) demonstrate the evolution of In $3d_{5/2}$ under various experimental conditions recorded on In_2O_3 and InZr_7.1, respectively. The positions of In-In, InO_x, and In_2O_3 are marked in the figures as vertical dashed lines. The slightly broadened photoemission spectra in b) at low temperature was a result of surface charging effect, which was eliminated at increased temperatures. The APXPS experiments were performed in 0.1 Torr CO_2 and 0.4 Torr of H_2 (reaction atmosphere, RXN) under different temperatures. The photoemission spectra were plotted from bottom to top as a function of the order the experiments were performed. The same experimental conditions in the labels were conducted to investigate the reversibility of the redox behavior of surface In atoms. Note that, although the nominal experimental conditions were identical for some cases, the "history" of the catalyst was different. The evolution of surface Zr/In atomic ratios for InZr_2.5 and InZr_7.1 catalysts under various experimental conditions are shown in c). The 1-14 experimental conditions shown in x-axis of c) correspond to RXN (RT, 1), RXN (523, 573, 623, 673 K, 2-5), RXN (523, 573, 623, 673 K, 6-9), RXN (523, 573, 623, 673 K, 10-13), and 0.1 Torr O_2 (573 K, 14). d) Fitted In 3d photoemission spectra recorded on In_2O_3 and InZr_7.1 obtained at 573 K.

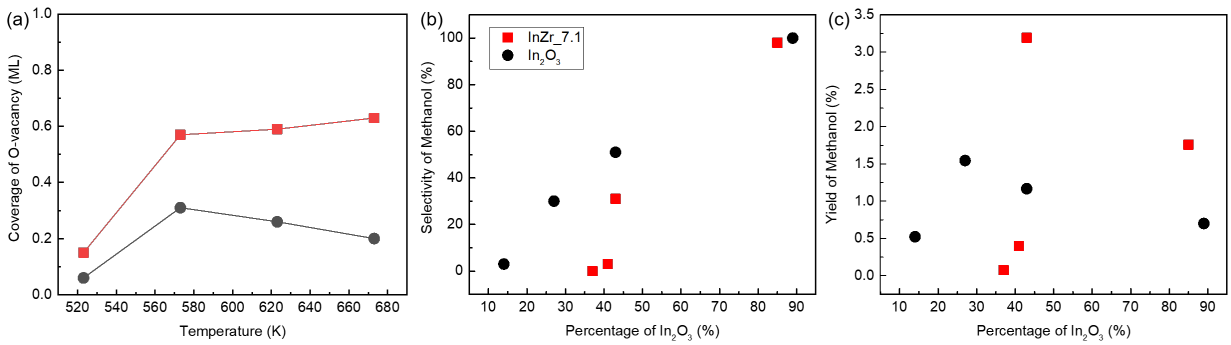

Fig. 4 Evolution of the coverage of surface oxygen vacancy as a function temperature (a) in the reaction atmosphere (0.1 Torr CO_2 and 0.4 Torr of H_2), and the relationship between the percentages of surface In_2O_3 (*at* %) and S_{CH3OH} (b) and Y_{CH3OH} (c) for In_2O_3 and InZr_7.1. The coverage of oxygen vacancy, percentage values of In_2O_3 and In^0 were obtained by fitting corresponding photoemission spectra of In $3d_{5/2}$. The catalysis data, including S_{CH3OH} (b) and Y_{CH3OH} (c) were extracted from the catalysis measurements shown in Fig. 2. Note that, although

the reaction atmosphere was the same between APXPS and catalysis experiments, there was still significant pressure gaps between the two experiments.

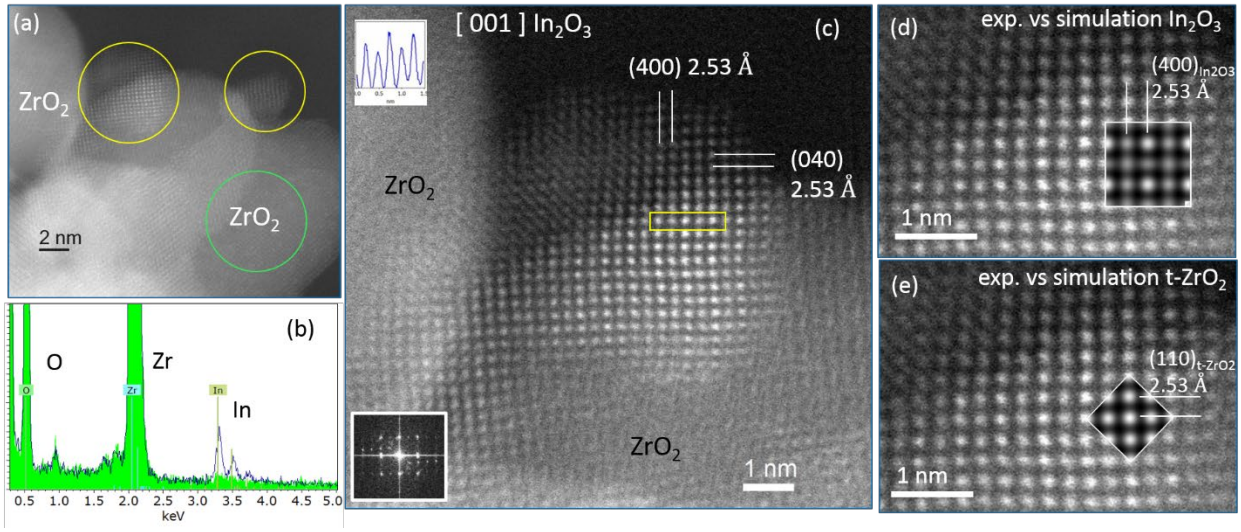

Fig. 5 TEM characterizations of spent InZr_7.1 and the stabilized In_2O_3 via interactions with *m*-ZrO_2. a) Representative HAADF-STEM image with different In concentrations highlighted (yellow indicates higher levels of In and green indicates lower levels of In); b) Corresponding EDS spectra of highlighted regions in a); c) HAADF-STEM image of the highlighted nanostructure in a) and the analysis of inter-plane spacings / line profiles across lattice fringes (top left inset, correspond to the rectangular-highlighted region) & FFT image (bottom left). The image noise was reduced by summing original image and the Fourier-filtered image; d) Experiment vs simulation for [001] In_2O_3 (1 unit cell); e) Experiment vs simulation for *t*-ZrO_2 [001] (2x2 unit cells). The following parameters were used for both STEM simulations, 200keV, Cs = 0.003mm, t = 100Å, HAADF angle 70-200mrad.

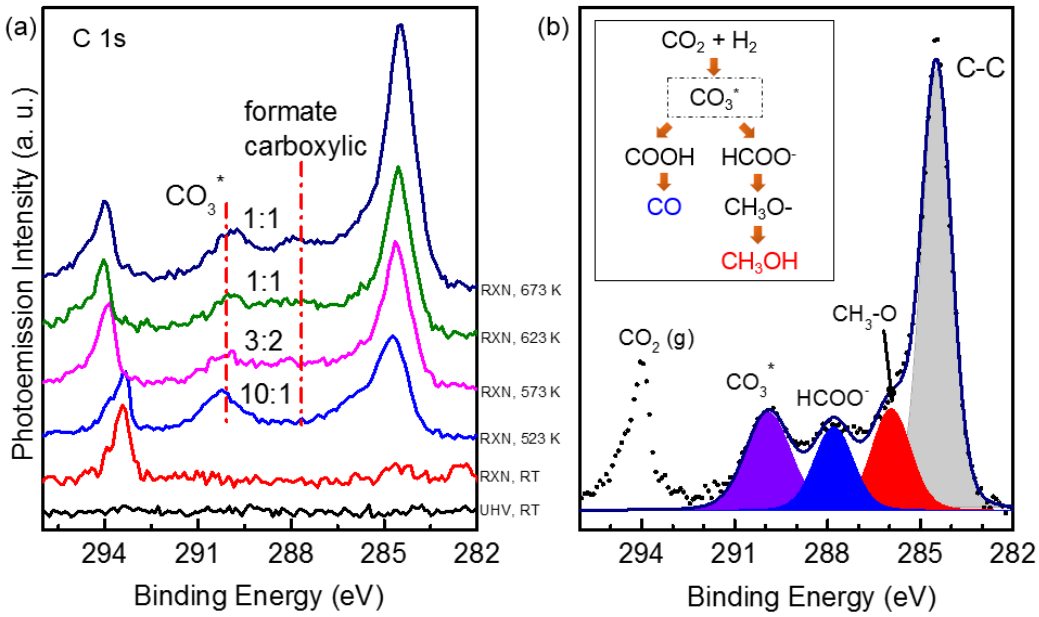

Fig. 6 The observation of reaction intermediates by APXPS under *in situ* conditions. a) Evolution of C 1s photoemission spectra of InZr_7.1 under different reaction conditions, where the BEs of CO_3^* and formate are highlighted as vertical lines; b) Fitting of representative C 1s photoemission spectra and quantifications, together with a proposed general reaction pathway under *in situ* conditions. The APXPS experiments were performed in 0.1 Torr CO_2 and 0.4 Torr of H_2 (reaction atmosphere, RXN). Signal from gaseous CO_2 contributes to a peak at ~294 eV with different binding energies under various reaction conditions, as a result of changed surface work functions of the catalyst.

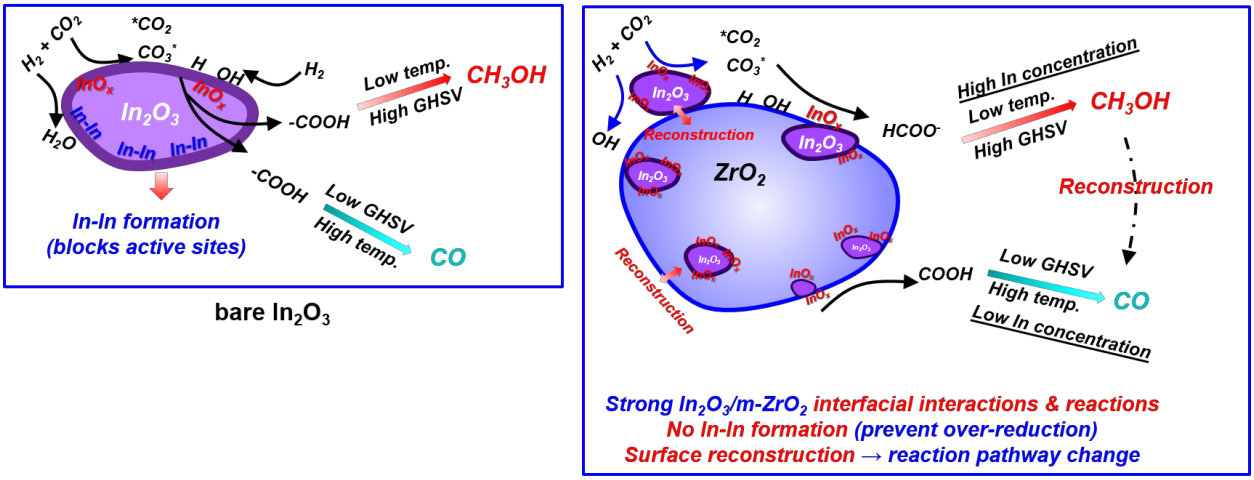

Fig. 7 Cartoons summarizing the chemical and structural characteristics of different In_2O_3-based catalysts under *in situ* conditions.

TOC

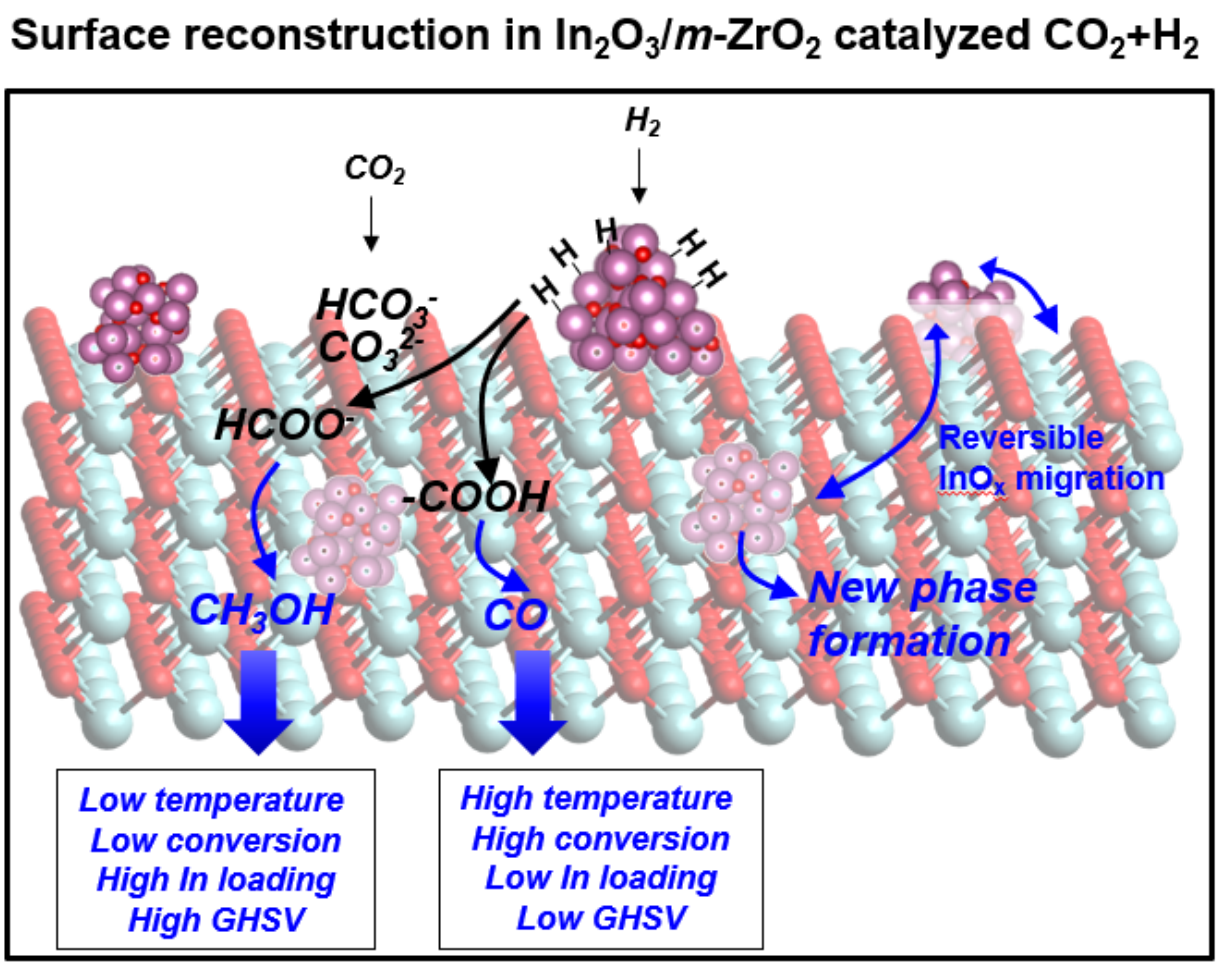
Surface reconstruction in In_2O_3/m-ZrO_2 catalyzed CO_2+H_2
CO_2
H_2
HCO_3^-
CO_3^{2-}
$HCOO^-$
-COOH
CH_3OH
CO
Reversible
InO_x migration
New phase
formation
Low temperature
Low conversion
High In loading
High GHSV
High temperature
High conversion
Low In loading
Low GHSV

References

(1) Li, K. Z.; Chen, J. G. CO_2 Hydrogenation to Methanol over ZrO_2-Containing Catalysts: Insights into ZrO_2 Induced Synergy. *ACS Catal.* **2019**, *9*, 7840-7861.
(2) Jiang, X.; Nie, X.; Guo, X.; Song, C.; Chen, J. Recent Advances in Carbon Dioxide Hydrogenation to Methanol Via Heterogeneous Catalysis. *Chem. Rev.* **2020**, 15, 7984–8034.
(3) Wang, J. J.; Li, G. N.; Li, Z. L.; Tang, C. Z.; Feng, Z. C.; An, H. Y.; Liu, H. L.; Liu, T. F.; Li, C. A Highly Selective and Stable ZnO-ZrO_2 Solid Solution Catalyst for CO_2 Hydrogenation to Methanol. *Sci. Adv.* **2017**, *3*, sciadv.1701290.
(4) Studt, F.; Behrens, M.; Kunkes, E. L.; Thomas, N.; Zander, S.; Tarasov, A.; Schumann, J.; Frei, E.; Varley, J. B.; Abild-Pedersen, F.; Norskov, J. K.; Schlogl, R. The Mechanism of CO and CO_2 Hydrogenation to Methanol over Cu-Based Catalysts. *ChemCatChem* **2015**, *7*, 1105-1111.
(5) Martin, O.; Martin, A. J.; Mondelli, C.; Mitchell, S.; Segawa, T. F.; Hauert, R.; Drouilly, C.; Curulla-Ferre, D.; Perez-Ramirez, J. Indium Oxide as a Superior Catalyst for Methanol Synthesis by CO_2 Hydrogenation. *Angew. Chem. Int. Ed.* **2016**, *55*, 6261-6265.
(6) Frei, M. S.; Capdevila-Cortada, M.; Garcia-Muelas, R.; Mondelli, C.; Lopez, N.; Stewart, J. A.; Ferre, D. C.; Perez-Ramirez, J. Mechanism and Microkinetics of Methanol Synthesis via CO_2 Hydrogenation on Indium Oxide. *J. Catal.* **2018**, *361*, 313-321.
(7) Skrzypek, J.; Lachowska, M.; Serafin, D. Methanol Synthesis from CO_2 and H_2 Dependence of Equilibrium Conversions and Exit Equilibrium Concentrations of Components on the Main Process Variables. *Chem. Eng. Sci.* **1990**, *45*, 89-96.
(8) Sun, K. H.; Fan, Z. G.; Ye, J. Y.; Yan, J. M.; Ge, Q. F.; Li, Y. N.; He, W. J.; Yang, W. M.; Liu, C. J. Hydrogenation of CO_2 to Methanol over In_2O_3 Catalyst. *J. CO_2 Util.* **2015**, *12*, 1-6.
(9) Ye, J. Y.; Liu, C. J.; Mei, D. H.; Ge, Q. F. Active Oxygen Vacancy Site for Methanol Synthesis from CO_2 Hydrogenation on In_2O_3(110): A DFT Study. *ACS Catal.* **2013**, *3*, 1296-1306.
(10) Ye, J. Y.; Liu, C. J.; Ge, Q. DFT Study of CO_2 Adsorption and Hydrogenation on the In_2O_3 Surface. *J. Phys. Chem. C* **2012**, *116*, 7817-7825.
(11) Rui, N.; Wang, Z. Y.; Sun, K. H.; Ye, J. Y.; Ge, Q. F.; Liu, C. J. CO_2 Hydrogenation to Methanol over Pd/In_2O_3: Effects of Pd and Oxygen Vacancy. *Appl. Catal. B: Environ.* **2017**, *218*, 488-497.
(12) Ye, J. Y.; Liu, C. J.; Mei, D. H.; Ge, Q. F. Methanol Synthesis from CO_2 Hydrogenation over a Pd_4/In_2O_3 Model Catalyst: A Combined DFT and Kinetic Study. *J. Catal.* **2014**, *317*, 44-53.
(13) Frei, S. M.; Mondelli, C.; Cesarini, A.; Krumeich, F.; Hauert, R.; Ferre, D. C.; Perez-Ramirez, J. Role of Zirconia Carrier on Indium Oxide-Catalyzed CO_2 Hydrogenation to Methanol. *ACS Catal.* **2019**, 2020, 10, 1133–1145.
(14) Chou, C. Y.; Lobo, R. F. Direct Conversion of CO_2 into Methanol over Promoted Indium Oxide-Based Catalysts. *Appl. Catal. A: Gen.* **2019**, *583*, 9.
(15) Chen, T. Y.; Cao, C. X.; Chen, T. B.; Ding, X. X.; Huang, H.; Shen, L.; Cao, X. Y.; Zhu, M. H.; Xu, J.; Gao, J.; Han, Y. F. Unraveling Highly Tunable Selectivity in CO_2 Hydrogenation over Bimetallic In-Zr Oxide Catalysts. *ACS Catalysis* **2019**, *9*, 8785-8797.
(16) Snider, J. L.; Streibel, V.; Hubert, M. A.; Choksi, T. S.; Valle, E.; Upham, D. C.; Schumann, J.; Duyar, M. S.; Gallo, A.; Abild-Pedersen, F.; Jaramillo, T. F. Revealing the Synergy between Oxide and Alloy Phases on the Performance of Bimetallic In-Pd Catalysts for CO_2 Hydrogenation to Methanol. *ACS Catal.* **2019**, *9*, 3399-3412.

(17) Dou, M. B.; Zhang, M. H.; Chen, Y. F.; Yu, Y. Z. DFT Study of In_2O_3-Catalyzed Methanol Synthesis from CO_2 and CO Hydrogenation on the Defective Site. *New J. Chem.* **2018**, *42*, 3293-3300.
(18) Dang, S. S.; Qin, B.; Yang, Y.; Wang, H.; Cai, J.; Han, Y.; Li, S. G.; Gao, P.; Sun, Y. H. Rationally Designed Indium Oxide Catalysts for CO_2 Hydrogenation to Methanol with High Activity and Selectivity. *Sci. Adv.* **2020**, *6*, eaaz2060.
(19) Bavykina, A.; Yarulina, I.; Al Abdulghani, A. J.; Gevers, L.; Hedhili, M. N.; Miao, X. H.; Galilea, A. R.; Pustovarenko, A.; Dikhtiarenko, A.; Cadiau, A. et al. Turning a Methanation Co Catalyst into an In-Co Methanol Producer. *ACS Catal.* **2019**, *9*, 6910-6918.
(20) Wang, L. R.; Cai, J. Y.; Xie, Y.; Guo, J. S.; Xu, L. X.; Yu, S. Y.; Zheng, X. S.; Ye, J.; Zhu, J. F.; Zhang, L. J. et al. In_2O_3 Nanocrystals for CO_2 Fixation: Atomic-Level Insight into the Role of Grain Boundaries. *iScience* **2019**, *16*, 390-398.
(21) Li, M. M. J.; Zou, H. B.; Zheng, J. W.; Wu, T. S.; Chan, T. S.; Soo, Y. L.; Wu, X. P.; Gong, X. Q.; Chen, T. Y.; Roy, K.; Held, G.; Tsang, S. C. E. Methanol Synthesis at a Wide Range of H_2/CO_2 Ratios over a Rh-In Bimetallic Catalyst. *Angew. Chem. Int. Ed.* **2020**, *59*, 16039-16046
(22) Wang, J. Y. Z., G. H.; Zhu, J.; Zhang, X. B.; Ding, F. S.; Zhang, A. F.; Guo, X. W.; Song, C. S. CO_2 Hydrogenation to Methano over In_2O_3-Based Catalysts: From Methanesm to Catalyst Development. *ACS Catal.* 2021, *11*, 1406-1423.
(23) Cao, A. W., Z. B.; Li, H.; Norskov, J. K. . Relations between Surface Oxygen Vacancies and Activity of Methanol Formation from CO_2 Hydrogenation over In_2O_3 Surfaces. *ACS Catal.* 2021, *11*, 1780-1786.
(24) Yang, C. S.; Pei, C. L.; Luo, R.; Liu, S. H.; Wang, Y. N.; Wang, Z. Y.; Zhao, Z. J.; Gong, J. L. Strong Electronic Oxide–Support Interaction over In_2O_3/ZrO_2 for Highly Selective CO_2 Hydrogenation to Methanol. *J. Am. Chem. Soc.* **2020**, *142*, 19523-19531.
(25) Araujo, T. P.; Shah, A.; Mondelli, C.; Stewart, J. A.; Curulla Ferre, D.; Perez-Ramirez, J. Impact of Hybrid CO_2-CO Feeds on Methanol Synthesis over In_2O_3-Based Catalysts. *Appl. Catal. B: Environ.* **2021**, https://doi.org/10.1016/j.apcatb.2021.119878.
(26) Yang, C. S. P., C. L.; Luo, R.; Liu, S. H.; Wang Y. N.; Wang, Z. Y.; Zhao, Z. J.; Gong, J. L. Strong Electronic Oxide-Support Interaction over In_2O_3/ZrO_2 for Highly Selective CO_2 Hydrogenation to Methanol. *J. Am. Chem. Soc.* **2020**, *142*, 19523-19531.
(27) Rui, N.; Zhang, F.; Sun, K.; Liu, Z.; Xu, W.; Stavitski, E.; Senanayake, S. D.; Rodriguez, J. A.; Liu, C.-J. Hydrogenation of Co2 to Methanol on a Auδ+In2o3-X Catalyst. *ACS Catal.* **2020**, *10*, 11307-11317.
(28) Tsoukalou, A.; Abdala, P. M.; Stoian, D.; Huang, X.; Willinger, M. G.; Fedorov, A.; Muller, C. R. Structural Evolution and Dynamics of an In_2O_3 Catalyst for CO_2 Hydrogenation to Methanol: An *Operando* XAS-XRD and *in-situ* TEM Study. *J. Am. Chem. Soc.* **2019**, *141*, 13497-13505.
(29) Da S. Bronsato, B. J. Z., P. C.; Moreira, C. R.; Mendoza, C. D.; Maia da Costa, M. E. H.; Alves, O. C.; De Avillez, R. R.; Appel, L. G. How the Interaction between In2o3-Zro2 Promotes the Isobutene Synthesis from Ethanol. *Catal. Today* **2020**, https://doi.org/10.1016/j.cattod.2020.07.004.
(30) Turner, H. W.; Volpe, A. F.; Weinberg, W. H. High-Throughput Heterogeneous Catalyst Research. *Surf. Sci.* **2009**, *603*, 1763-1769.
(31) Bluhm, H.; Andersson, K.; Araki, T.; Benzerara, K.; Brown, G. E.; Dynes, J. J.; Ghosal, S.; Gilles, M. K.; Hansen, H. C.; Hemminger, J. C. et al. Soft X-Ray Microscopy and Spectroscopy at the Molecular Environmental Science Beamline at the Advanced Light Source. *J. Electron Spectros. Relat. Phenomena* **2006**, *150*, 86-104.

(32) Ogletree, D. F.; Bluhm, H.; Lebedev, G.; Fadley, C. S.; Hussain, Z.; Salmeron, M. A Differentially Pumped Electrostatic Lens System for Photoemission Studies in the Millibar Range. *Rev. Sci. Instrum.* **2002**, *73*, 3872-3877.
(33) Ravel, B.; Newville, M. Athena, Artemis, Hephaestus: Data Analysis for X-Ray Absorption Spectroscopy Using IFEFIT. *J. Synchrot. Radiat.* **2005**, *12*, 537-541.
(34) Emeline, A.; Kataeva, G. V.; Litke, A. S.; Rudakova, A. V.; Ryabchuk, V. K.; Serpone, N. Spectroscopic and Photoluminescence Studies of a Wide Band Gap Insulating Material: Powdered and Colloidal ZrO_2 Sols. *Langmuir* **1998**, *14*, 5011-5022.
(35) King, P. D. C.; Veal, T. D.; Fuchs, F.; Wang, C. Y.; Payne, D. J.; Bourlange, A.; Zhang, H.; Bell, G. R.; Cimalla, V.; Ambacher, O.; Egdell, R. G.; Bechstedt, F.; McConville, C. F. Band Gap, Electronic Structure, and Surface Electron Accumulation of Cubic and Rhombohedral In_2O_3. Phys. Rev. B 2009, 79, 205211.
(36) Suzuki, T.; Watanabe, H.; Ueno, T.; Oaki, Y.; Imai, H. Significant Increase in Band Gap and Emission Efficiency of In_2O_3 Quantum Dots by Size-Tuning around 1 nm in Supermicroporous Silicas. Langmuir 2017, 33, 3014-3017.
(37) P. Erhart, A. K., R.G. Egdell, K. Albe. Band Structure of Indium Oxide: Indirect Versus Direct Band Gap. Phys. Rev. B 2007, 75, 153205
(38) V. Scherer, C. J., A. Krapf, H. Dwelk, D. Braun, R. Manzke. Transport and Angular Resolved Photoemission Measurements of the Electronic Properties of In_2O_3 Bulk Single Crystals. Appl. Phys. Lett. 2012, 100, 212108.
(39) Mori, T.; Kajihara, K.; Kanamura, K.; Toda, Y.; Hiramatsu, H.; Hosono, H. Indium-Based Ultraviolet-Transparent Electroconductive Oxyfluoride Inof: Ambient-Pressure Synthesis and Unique Electronic Properties in Comparison with In_2O_3. *J. Am. Chem. Soc.* **2013**, *135*, 13080-13088.
(40) Zhang, X.; Ogitsu, T.; Wood, B. C.; Pham, T. A.; Ptasinska, S. Oxidation-Induced Polymerization of InP Surface and Implications for Optoelectronic Applications. *J. Phys. Chem. C* **2019**, *123*, 30893-30902.
(41) Brown, Z. L.; Jurng, S.; Lucht, B. L. Investigation of the Lithium Solid Electrolyte Interphase in Vinylene Carbonate Electrolytes Using Cu Parallel to $LiFePO_4$ Cells. *J. Electrochem. Soc.* **2017**, *164*, A2186-A2189.
(42) Favaro, M.; Xiao, H.; Cheng, T.; Goddard, W. A.; Yano, J.; Crumlin, E. J. Subsurface Oxide Plays a Critical Role in CO_2 Activation by Cu(111) Surfaces to Form Chemisorbed CO_2, the First Step in Reduction of CO_2. *PNAS* **2017**, *114*, 6706-6711.
(43) Li, M.; Luo, W.; Zuttel, A. Near Ambient-Pressure X-Ray Photoelectron Spectroscopy Study of Co2 Activation and Hydrogenation on Indium/Copper Surface. *J. Catal.* **2021**, *395*, 315-324.
(44) Detweiler, Z. M.; Wulfsberg, S. M.; Frith, M. G.; Bocarsly, A. B.; Bernasek, S. L. The Oxidation and Surface Speciation of Indium and Indium Oxides Exposed to Atmospheric Oxidants. *Surf. Sci.* **2016**, *648*, 188-195.
(45) Zhang, X.; Pham, T. A.; Ogitsu, T.; Wood, B. C.; Ptasinska, S. Modulation of Surface Bonding Topology: Oxygen Bridges on OH Terminated InP (001). *J. Phys. Chem. C* **2020**, *124*, 3196-3203.
(46) Tao, F.; Zhang, S. R.; Nguyen, L.; Zhang, X. Action of Bimetallic Nanocatalysts under Reaction Conditions and During Catalysis: Evolution of Chemistry from High Vacuum Conditions to Reaction Conditions. *Chem. Soc. Rev.* **2012**, *41*, 7980-7993.

(47) Linstrom, P. J.; Mallard, W. G.: *NIST Chemistry Webbook, NIST Standard Reference Database Number 69*; National Institute of Standards and Technology: Gaithersburg, MD, 2013; Vol. 20899.
(48) Jiang, N. Electron Beam Damage in Oxides: A Review. *Rep. Prog. Phys.* **2016**, *79*, 33.